

Article

Regulation of Calcium Source and Addition Method for MICP in Repairing High-Temperature Concrete Damage

Hong Wei ¹ , Yanan Fan ^{2,*}, Hongxiu Du ¹, Renwang Liang ^{1,*} and Xiaoyuan Wang ¹

¹ College of Civil Engineering, Taiyuan University of Technology, Taiyuan 030024, China; weihong0052@link.tyut.edu.cn (H.W.)

² Department of Architecture and Environmental Engineering, Taiyuan University, Taiyuan 030032, China

* Correspondence: 2022504101@tyu.edu.cn (Y.F.); lrw1962@163.com (R.L.)

Abstract: After exposure to high temperatures, the mechanical properties and durability of concrete structures are significantly reduced, and effective measures must be taken for reinforcement and repair. High-temperature concrete damage manifests as looseness, spalling, and cracks, which are suitable for microbial-induced carbonate precipitation. When repairing high-temperature concrete damage with microbial-induced carbonate precipitation (MICP), the calcium source is an important influencing factor. The type of calcium source and the method used to add calcium source will directly affect the mineralized products, which in turn affect the quality of the repair. In this study, the mineralized products of *Sporosarcina pasteurii* were qualitatively analyzed and the appropriate type of calcium source and addition method were determined. The repair effect on high-temperature concrete damage was also verified. The results showed that the mineralized products of *Sporosarcina pasteurii* were calcium carbonate, with mixed vaterite and calcite crystals. Calcium acetate was found to be the most appropriate calcium source, while the pre-calcium-source addition method was shown to be optimal. At each damage temperature, the compressive strength showed a certain degree of recovery, and the water absorption exhibited a certain degree of reduction. At 600 °C, the compressive strength of the repaired specimens increased up to 202.68% compared with the damaged specimens and the water absorption of the repaired specimens was 34.32% lower than that of the damaged specimens. The higher the damage temperature, the more obvious the repair effect.

Keywords: microbial-induced carbonate precipitation; calcium source; energy dispersive spectroscopy; X-ray diffraction; scanning electron microscope; compressive strength; water absorption



Citation: Wei, H.; Fan, Y.; Du, H.; Liang, R.; Wang, X. Regulation of Calcium Source and Addition Method for MICP in Repairing High-Temperature Concrete Damage. *Appl. Sci.* **2023**, *13*, 5528. <https://doi.org/10.3390/app13095528>

Academic Editors: Aldina Santiago, Nicola Tondini and Luis Laim

Received: 20 March 2023

Revised: 16 April 2023

Accepted: 26 April 2023

Published: 28 April 2023



Copyright: © 2023 by the authors. Licensee MDPI, Basel, Switzerland. This article is an open access article distributed under the terms and conditions of the Creative Commons Attribution (CC BY) license (<https://creativecommons.org/licenses/by/4.0/>).

1. Introduction

After exposure to high temperatures, the mechanical properties and durability of concrete structures will be affected to varying degrees. Wu et al. [1] tested the mechanical properties of C70 and C85 high-strength concrete (HSC) after high temperature, they found that the HSC specimens explosive spalled when heated to 500 °C, and the average compressive strength loss of the two kinds of HSC was 63.2% and 49.2%, respectively, at 500 °C. Gao et al. [2] measured the chloride ion permeability of C20, C40, and C60 concrete, the results showed that the chloride ion migration coefficient of concrete increased significantly with the increase of temperature, the chloride ion migration coefficient of C60 concrete specimens even reached $12.3 \times 10^{-12} \text{ m}^2/\text{s}$ at 800 °C. Du et al. [3] studied the mechanical properties and microstructure of C60 high-performance concrete (HPC) at 20~600 °C using X-ray computed tomography (X-CT) technology. They found that as the temperature increased, the compressive strength of HPC showed a decreasing trend. This was because the microstructure of concrete deteriorated with the increase in temperature, and the length, width, area, and girth of cracks exhibited an increasing trend.

In order to deal with high-temperature concrete damage, some researchers proposed reinforce or repair methods. Rabehi et al. [4] reinforced ordinary concrete (OC) and HPC

that have gone through fire by increasing cross-section method. The results showed that the compressive strength of HPC reinforced with carbon fiber cloth increased by 38%, while the HPC reinforced with fiber glass had an improvement of ductility while restoring its compressive strength. Chen et al. [5] prepared graphite oxide and silane composite solution to repair high-temperature damaged concrete. They found that the penetration depth of the composite solution in concrete reached more than 9 mm, and formed a certain thickness of hydrophobic layer, thus improved the impermeability of the damaged concrete.

The above reinforce and repair methods restored the performance of damaged concrete to some extent. However, the reinforce method increased the cross-section area and self-weight of the concrete components, while the repairing agents were prone to aging and had poor long-term performance.

High-temperature damage in concrete is the result of multi-factor and multi-scale damage that spreads from the surface to the center and mainly manifests as defects such as looseness, spalling and cracks [6]. When concrete is subjected to high temperatures, most of the resulting surface cracks are macroscopic; in particular, the number of cracks smaller than 1 mm increases significantly, and the interior of the concrete is loose and porous with 6–50 μm cracks [7]. Microbes, repair fluid and oxygen can easily enter the interior of the concrete through these cracks. Therefore, it is possible to introduce mineralizing microbes into damaged concrete within a specific repair fluid, where they can mineralize and deposit calcium carbonate (CaCO_3) crystals to fill the internal and surface defects, thus repairing the damaged concrete. This process of microbial mineralization is called MICP.

MICP is a mineralization reaction that involves the transformation of ions in solution into solid minerals under certain physical and chemical conditions and under the control of microbial organic substances at specific sites of microbes [8]. The mechanism is shown in Figure 1. The sediment produced by MICP is CaCO_3 , which has good compatibility with concrete and will not harm the environment in the repair process or with long-term service. NH_4^+ is the byproduct of MICP, which convert into NH_3 in the solution and then release into the atmosphere, however, NH_4^+ and NH_3 can be adsorbed by adding zeolite powder in the solution. Zeolite powder promotes the generation of struvite, which also have a certain hardness and strength [9]. Compared with traditional concrete defect repair methods, MICP has significant advantages and broad application prospects. In the past few decades, MICP—as a new technology—has been widely discussed by scholars. Many scholars have carried out exploratory studies on the application of MICP in several fields and have achieved certain results.

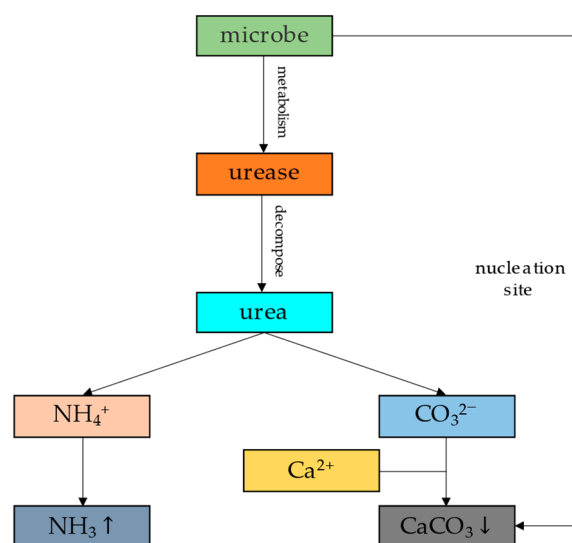


Figure 1. Mechanism of MICP.

Kong et al. [10] carried out sand stabilization and wind erosion experiments with *Sporosarcina pasteurii*, *Artemisia desertorum* and *Astragalus adsurgens*. Their results showed that when the concentration of consolidating fluid was 0.15 mol/L, the temperature was 20 °C and the concentration of bacterial fluid was $OD_{600} = 0.6$, MICP improved the wind erosion resistance of desert aeolian sand by 39.83%, while the combination of desert plants improved the wind erosion resistance up to 44.08%.

Li et al. [11] solidified zinc–lead composite heavy-metal-contaminated soil by combining MICP with adsorption materials. Their results showed that MICP effectively reduced the leachability of heavy metal in contaminated soil; the unconfined compression strength of the samples increased by 8.3% with the addition of 10% porous silicon, while the leaching concentration of lead decreased by 67.81% and that of zinc decreased by 63.4%.

Zhu [12] carried out a mineralization test on the surface of stone materials using carbonate-mineralizing bacteria. The results showed that a dense mineralized film formed on the surface of sandstone and marble when using immersion and brushing methods, where the mineralized crystals were calcite and vaterite. The mineralized film was found to resist erosion caused by acid rain and showed good heat, aging, and frost resistance. The impermeability of the stone was also significantly improved.

Wang et al. [13] studied the use of microencapsulated bacteria for concrete self-repair. Their results showed that the repair rate of the samples with bacterial microcapsules was higher than that of the samples without bacterial microcapsules. In addition, the maximum crack width repaired by bacterial microcapsules was 970 μm —almost four times that of the non-bacterial groups—while the water permeability of the bacterial groups was about 10 times lower than that of the non-bacterial groups.

Concrete self-repair technologies allow concrete structures to become multifunctional and intelligent to a certain extent, it seems to be an ideal method for repairing high-temperature concrete damage. However, self-repair technologies require the mineralizing bacteria to be mixed into the concrete, the mineralizing bacteria cannot withstand high temperatures at all. That is, when repairing high-temperature concrete damage, self-repair technologies are not applicable—only passive repair technologies can be adopted.

Passive repair technologies refer to the protection of surface defects and repair of cracks by artificially providing suitable conditions for MICP after concrete cracking. For existing cracks in concrete, MICP can generate a layer of CaCO_3 mineralized film on the surface of the concrete to block surface defects [14], and some mineralizing bacteria and repair fluid can even penetrate concrete to fill internal defects. The mechanism is shown in Figure 2.

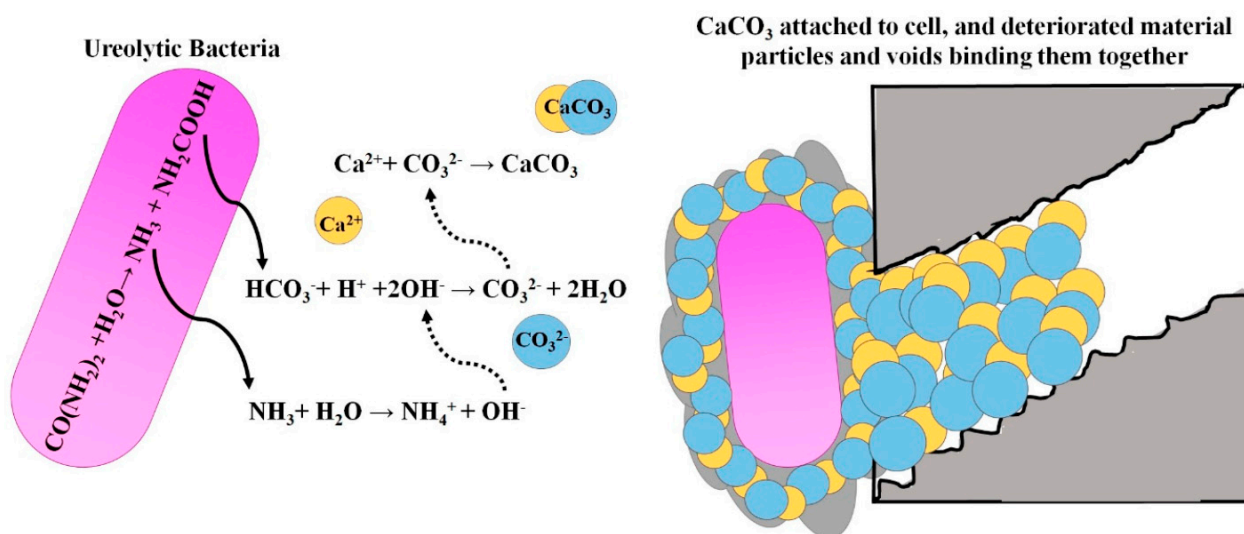


Figure 2. Passive repair of concrete defects by MICP [14].

Zhang [15] carried out an experimental study on surface filming and passive crack repair in cement mortar specimens using MICP. The results showed that cracks with a width of 0.2~0.4 mm could be repaired by the grouting method, and the flexural strength of the repaired specimens was about 200 kPa. After coating the surface of the specimens by the brushing method, the water absorption of the specimens decreased by 10%. In addition, Zhang also carried out a field test with MICP for controlling leakage in a basement. The results showed that a large amount of CaCO_3 was generated in the cracks, and the cracks were completely covered by CaCO_3 film. Four months after repair, there was no rainwater seepage in the cracks.

A few studies have confirmed the feasibility of repairing high-temperature concrete damage using MICP. Fan [16] carried out experimental research on repairing high-temperature concrete damage using MICP. The results showed that after repair, the surface cracks on the damaged specimens were all covered, the water absorption rate was reduced to its pre-damage state, the chloride ion migration coefficient decreased up to 60.6%, the compressive strength increased by 42% and the porosity decreased by 12.9%.

At present, research on MICP for passive repair has mainly focused on windbreak, sand fixation, heavy-metal-contaminated soil treatment and the repair of cultural relics. However, there are very little research on MICP in repairing high-temperature concrete damage. The influences of calcium source types and calcium source addition methods on MICP are rarely reported. There are almost no analyses on the regulatory mechanism of calcium source types and calcium source addition methods on the mineralization products of MICP. This study has guiding significance for the application of MICP in repairing high-temperature concrete damage.

The essence of MICP is that microbes continuously secrete urease from their metabolic processes; urease decomposes urea in the surrounding environment and CO_3^{2-} combines with the surrounding Ca^{2+} to form CaCO_3 deposits. For MICP, the Ca^{2+} source in the mineralizing environment is a very important influencing factor, and the type of Ca^{2+} source and method of addition will greatly affect the production, phase, morphology, structure, etc., of the mineralized products, which will, in turn, affect the quality of the repair.

In this study, whether *Sporosarcina pasteurii* could mineralize and deposit CaCO_3 under conditions where urea and Ca^{2+} sources exist in the surrounding environment was explored; then, a qualitative analysis of the mineralized products was carried out. By changing the type of Ca^{2+} source and the method of Ca^{2+} addition, the productivity, material, phase, morphology, and structure of the mineralized products were determined using weighing, multi-parameter analyzer, X-ray diffraction (XRD), energy dispersive spectrometry (EDS), scanning electron microscopy (SEM) and other testing methods. In this way, the appropriate type of Ca^{2+} source and method of Ca^{2+} addition was determined. Finally, the repair effect on high-temperature concrete damage was verified.

2. Microbial Induced Carbonate Precipitation by *Sporosarcina pasteurii*

There are various urease-producing bacteria in nature, and their characteristics are different [8,17], as shown in Table 1.

Table 1. Characteristics of different urease-producing bacteria.

Microorganism	Urease Activity	Basophilic	Aerobic	Pathogenic
<i>Sporosarcina pasteurii</i>	high	✓	✓	✗
<i>Proteus vulgaris</i>	low	moderate	✓	moderate
<i>Proteus mirabilis</i>	low	moderate	✓	✓
<i>Helicobacter pylori</i>	high	✗	✓	✓

After exposure to high temperatures, concrete becomes porous, has strong alkalinity and many cracks, and the cracks are rich in oxygen. For the application purpose of this article, the ideal urease-producing bacteria should have the following characteristics: (1) Adaptability to the alkaline environment; (2) Aerobic, microaerobic, or facultative

anaerobic; (3) Secrete high activity urease; (4) Bacteria and their metabolites are non-toxic, harmless, and non-pathogenic.

Previous research [8,17] showed that *Sporosarcina pasteurii* can survive in a weak alkaline environment and produce high activity urease, they are aerobic bacteria, and the bacteria themselves and their metabolites are non-toxic, harmless, and non-pathogenic. In conclusion, *Sporosarcina pasteurii* is the ideal urease-producing bacteria.

Sporosarcina pasteurii can secrete urease during its metabolic process; this urease will decompose urea in the surrounding environment into NH_4^+ and CO_3^{2-} , then mineralize and deposit CaCO_3 in the presence of Ca^{2+} .

2.1. Qualitative Analysis of Mineralized Products

An aliquot of 1 mol/L urea solution was added into a conical flask. *Sporosarcina pasteurii*, cultured for 24 h, was added into the conical flask at a volume of 10%. Then, the initial pH value of the mixed solution was adjusted to 8.0, the temperature was set to 30 °C, the rotating speed was set to 150 r/min and the conical flask was put in a shaking table for 24 h. After removing the conical flask from the shaking table, 1 mol/L CaCl_2 solution was added. The mixed solution became turbid rapidly and a large number of white suspended pastes appeared. After standing for an hour, the white suspended pastes were deposited at the bottom of the conical flask, as shown in Figure 3. The white sediments were then filtered and dried to produce white powders, and portions of the white sediments were prepared for EDS, SEM, and XRD analyses.

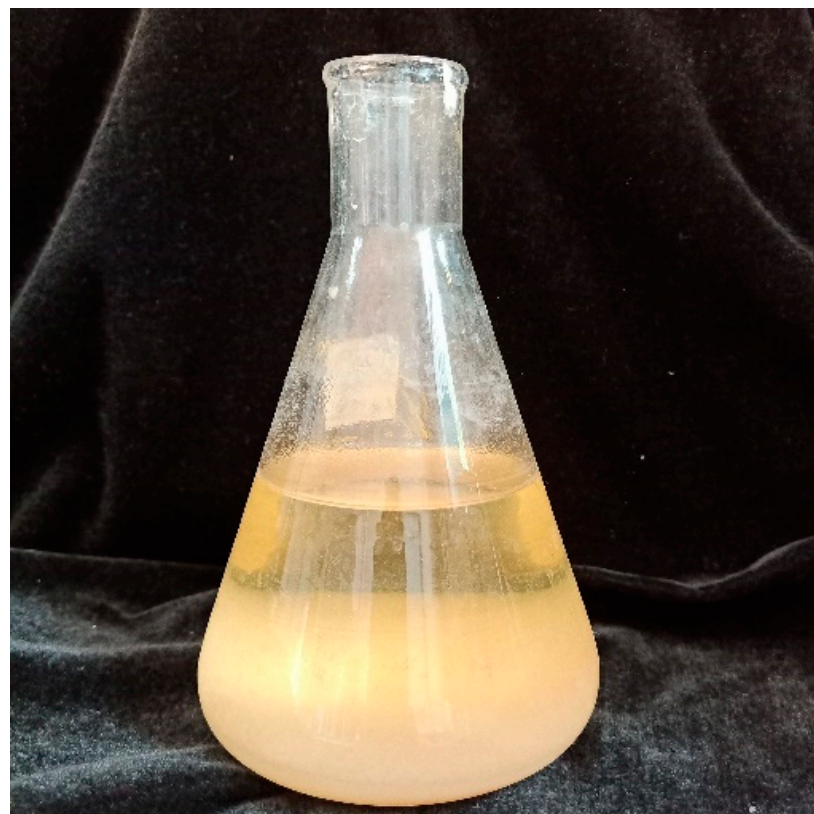


Figure 3. Mineralization and precipitation of *Sporosarcina pasteurii*.

2.1.1. EDS and SEM Analyses

The sample was pasted on the testing table with conductive adhesive and sprayed with gold for 60 s before observation with a TESCAN-LYRA3 scanning electron microscope. At the same time, the sample was analyzed using an Xplore30 energy spectrometer integrated into the SEM; the acceleration voltage of the SEM was 0.5~30 kV and the magnification was

5~100,000 \times . The energy spectrum of the sample is shown in Figure 4 and the SEM images are shown in Figure 5.

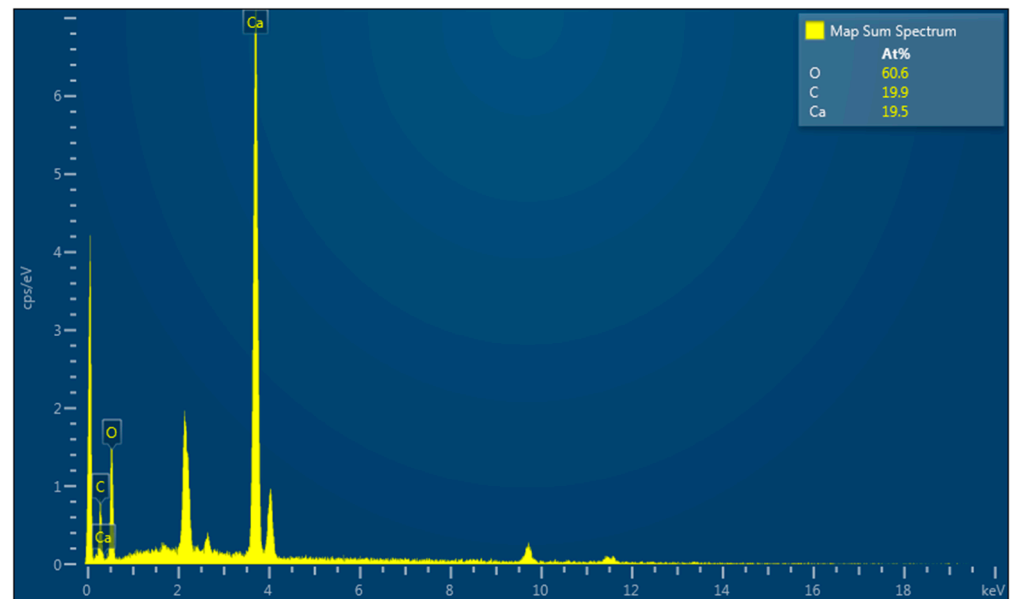
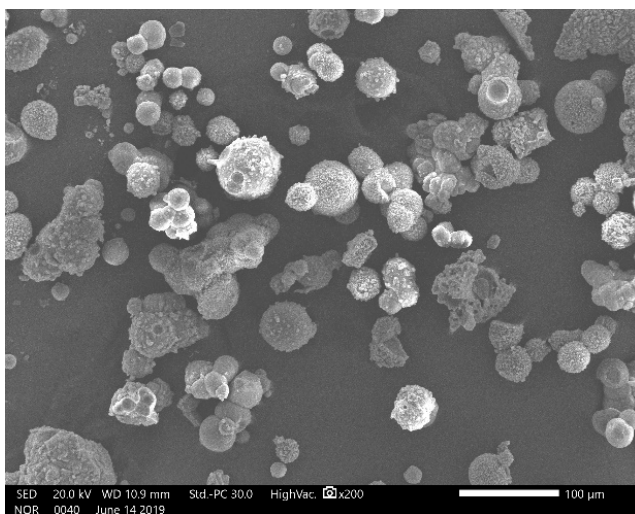


Figure 4. The energy spectrum of sediments.



(a)



(b)

Figure 5. SEM images of sediments. **(a)** Sediment crystals. **(b)** *Sporosarcina pasteurii* adhering to the surface of the crystals.

It can be seen from Figure 4 that the sample contained Ca, C, and O, and the atomic ratio of the three chemical elements was close to Ca:C:O = 1:1:3; thus, the mineralized products were CaCO₃.

It can be seen from Figure 5a that most of the mineralized product crystals were spheres; some were a single sphere, some were twin spheres and others were spherical aggregates. The diameter of the spheres ranged from 5 to 50 μ m, there were also some crystals with irregular shapes. There were some rods on the surface of the crystals with lengths around 1~2 μ m and diameters of 0.5 μ m; these were likely *Sporosarcina pasteurii* attached to the surface of the crystals, as seen in Figure 5b.

2.1.2. XRD Analysis

The sample was ground into powders with a mortar and screened with a 200-mesh sieve, then a test piece with a flat surface was created. The test piece was then analyzed using an Ultima IV X-ray diffractometer. The detailed parameters of XRD are shown in Table 2. The XRD spectrogram of the sample is shown in Figure 6.

Table 2. Detailed parameters of X-ray diffractometer.

X-ray Diffractometer Type	X-ray Wavelength	Working Voltage	Working Current	Scan Step	Scan Speed	Scan Range
Ultima IV	1.54056 Å	40 kV	40 mA	0.06°	4°/min	5~80°

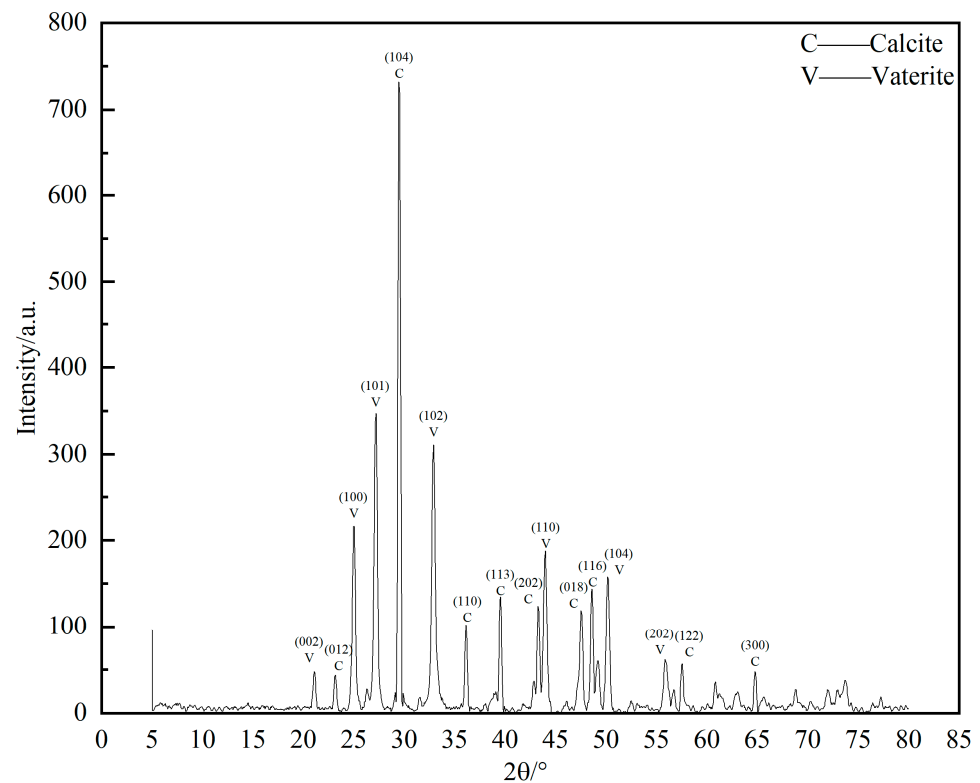


Figure 6. XRD spectrogram of sediments.

It can be seen from Figure 6 that the sample had two crystal forms. One crystal form exhibited characteristic diffraction peaks at $2\theta = 20.909^\circ, 24.873^\circ, 27.029^\circ, 32.713^\circ, 43.804^\circ, 49.015^\circ, 49.922^\circ, \text{ and } 55.729^\circ$, corresponding to the crystal planes (002), (100), (101), (102), (110), (112), (104) and (202), respectively, which is consistent with the standard spectrum of vaterite (Mineral Power Diffraction File Data Book ICCD No. 33-268). The other crystal form had characteristic diffraction peaks at $2\theta = 23.059^\circ, 29.404^\circ, 35.980^\circ, 39.419^\circ, 43.171^\circ, 47.508^\circ, 48.513^\circ, 57.416^\circ \text{ and } 64.681^\circ$, corresponding to the crystal planes (012), (104), (110), (113), (202), (018), (116), (122) and (300), respectively, which is consistent with the standard spectrum of calcite (Mineral Power Diffraction File Data Book ICCD No. 05-0586). Therefore, the mineralized products were mixed with vaterite and calcite crystals.

2.2. Type of Crystalline CaCO_3

Crystalline CaCO_3 can be divided into tripartite, rhombic and hexagonal crystal systems. There are three common crystal forms, calcite, aragonite, and vaterite.

Calcite, the most stable crystal form of CaCO_3 , belongs to the tripartite crystal system. Calcite crystals have various morphologies; their aggregates can be clustered, granular,

massive, fibrous, bell emulsion, or earthy, and most show parallel columnar, platy, rhombus, or ditrigonal scalenohedron development in various states [18].

Aragonite is a metastable crystal form of CaCO_3 that belongs to the rhombic crystal system. Aragonite crystals are columnar or lance-shaped and often present as pseudo-hexagonal symmetric triplets [19].

Vaterite, the most unstable crystal form of CaCO_3 , belongs to the hexagonal crystal system. Vaterite is rare in nature, and it often exists in the form of hexagonal flakes or spherical aggregates in laboratory settings. Vaterite may also take on additional shapes such as discs, thin flakes, hexagons, etc. [20,21].

2.3. Crystallization of CaCO_3

The dissolution or precipitation of CaCO_3 crystals in the mixed solution can be explained by Gibbs Free Energy Theory [22,23]. The following reaction, shown in Formula (1), occurs in the CaCO_3 solution:



According to Phase Transformation Theory, the direction of phase transformation is always from the phase with higher chemical potential to the phase with lower chemical potential, that is, towards the direction of a decrease in chemical potential. Therefore, chemical potential can be regarded as the driving force of the transformation of substances from one phase to another. For any chemical reaction, the Gibbs free energy can be expressed by the Van't Hoff Isothermal Equation, as shown in Equations (2) and (3) below:

$$\Delta_r G_m = \Delta_r G_m^\ominus + RT \ln Q_\alpha \quad (2)$$

$$Q_\alpha = \frac{\alpha_{\text{Ca}^{2+}} \cdot \alpha_{\text{CO}_3^{2-}}}{\alpha_{\text{CaCO}_3}} \prod \alpha \quad (3)$$

where $\Delta_r G_m^\ominus$ is the change of the standard molar Gibbs free energy in the reaction, Q_α is the activity quotient, α is the activity of the substance or ion in the reaction, R is the partial molar quantity and T is the temperature.

When the reaction is in equilibrium, $\Delta_r G_m = 0$, $\Delta_r G_m^\ominus = -RT \ln Q_\alpha = -RT \ln K_{sp}$, where K_{sp} is the solubility product. At this time, the ion concentration is the largest and the solution is saturated. Another expression of the Van't Hoff Isothermal Equation can be obtained by transforming Equation (2), as shown in Equation (4):

$$\Delta_r G_m = RT \ln Q_\alpha - RT \ln K_{sp} = RT \ln \frac{Q_\alpha}{K_{sp}} \quad (4)$$

When $Q_\alpha > K_{sp}$, the reaction in Formula (1) proceeds to the left, the mixed solution is supersaturated and CaCO_3 crystals are deposited. When $Q_\alpha < K_{sp}$, the reaction in Formula (1) proceeds to the right, the solution is unsaturated and no crystals are deposited. When $Q_\alpha = K_{sp}$, the solution is saturated.

The dissolution or precipitation of CaCO_3 crystals in mixed solution also can be explained by Ion Activity Product Theory [24]. In the process of mineralization and deposition, tiny particles will be produced as the crystal nucleus; these tiny particles collide with each other continuously in the solution due to Brownian motion, resulting in the growth of CaCO_3 crystals on the surface of the crystal nucleus. In this process, supersaturation directly affects the formation of the CaCO_3 crystal nucleus and the growth of CaCO_3 crystals. The saturation coefficient (SI) of CaCO_3 reflects the trend of the deposition or dissolution of CaCO_3 crystals in the solution. The equation for SI is as follows:

$$SI = \sqrt{\frac{IAP}{K_{sp}}} \quad (5)$$

where IAP is the ion activity product, K_{sp} is the ion solubility product, $IAP_{CaCO_3} = \alpha_{Ca^{2+}} \cdot \alpha_{CO_3^{2-}}$, $\alpha_{Ca^{2+}}$ is the activity of Ca^{2+} , $\alpha_{CO_3^{2-}}$ is the activity of CO_3^{2-} and K_{spCaCO_3} is the solubility product of $CaCO_3$.

When $SI > 0$, the reaction tends to deposit $CaCO_3$ crystals; when $SI = 0$, the deposition and dissolution of $CaCO_3$ reach equilibrium; and when $SI < 0$, the reaction tends to dissolve $CaCO_3$ crystals.

The crystallization of $CaCO_3$ occurs through the following processes: First, *Sporosarcina pasteurii* secretes urease from its metabolic processes, which decomposes urea in the surrounding environment into NH_4^+ and CO_3^{2-} so that the solubility product of Ca^{2+} and CO_3^{2-} in the surrounding environment continues to accumulate and reach supersaturation. In order to restore equilibrium, the negatively charged *Sporosarcina pasteurii* adsorbs Ca^{2+} from the surrounding environment, which further increases the local CO_3^{2-} concentration. Ca^{2+} is continually adsorbed until the concentration of crystal precursors facilitates nucleation and the deposition of $CaCO_3$ crystals. With the continuous precipitation of $CaCO_3$ crystals and the continuous growth of the crystal nucleus, the Gibbs free energy of the system gradually decreases and returns to equilibrium, thus completing the precipitation process [25,26]. In the process described in Section 2.1, the Ca^{2+} source was added after the urea completely decomposed and the solubility product of Ca^{2+} and CO_3^{2-} in the mixed solution quickly reached supersaturation, resulting in instantaneous nucleation and deposition. Ca^{2+} was attracted uniformly in all directions; thus, the growth rates of crystals on different crystal planes were almost the same, and the $CaCO_3$ crystals were spheres.

3. Effect of Ca^{2+} Source and Addition Method on Mineralized Products

High-temperature concrete damage system contains a large amount of calcium oxide (CaO), which changes into calcium hydroxide ($Ca(OH)_2$) in a liquid environment. $Ca(OH)_2$ can theoretically provide Ca^{2+} for MICP, however, the solubility of $Ca(OH)_2$ in water at 30 °C is only 1.53 g/L, that is, 0.02 mol/L, the concentration of calcium source in this study should reach 0.5 mol/L. Only a small part of $Ca(OH)_2$ are dissolved in water, most of them are deposited in the form of lime slurry, which are semi-solid. The growth, reproduction, metabolism and mineralization of *Sporosarcina pasteurii* in lime slurry are limited. Due to the low solubility of $Ca(OH)_2$, the CaO in high-temperature damage system is not suitable for MICP. In order to achieve a better repair effect, Ca^{2+} must be introduced through additional Ca^{2+} sources.

3.1. Experimental Method

3.1.1. Weighing Method

The mineralized products were filtered using quantitative filter paper combined with vacuum filtration. Then, the mineralized products were dried to constant weight together with the filter papers and then weighed, from which the production of mineralized products was determined and the productivity was calculated.

3.1.2. Determination of Ca^{2+} Concentration

MICP leads to the mineralization and deposition of Ca^{2+} in the mineralizing system (the mixed solution containing *Sporosarcina pasteurii*, urea, and Ca^{2+} source) in the form of $CaCO_3$ crystals; thus, the concentration of Ca^{2+} in the mineralizing system decreases. Here, the concentration of Ca^{2+} in the mineralizing system before and after mineralization was measured using a multi-parameter analyzer combined with a PCA-1-01 calcium ion electrode in order to determine the utilization rate of the Ca^{2+} source, which indirectly reflects the mineralization efficiency.

3.1.3. EDS, XRD, and SEM Analyses

The testing method for EDS, XRD and SEM in this section is the same as that in Section 2.1. For details, please refer to Section 2.2.

3.1.4. Effect of Ca²⁺ Source and Addition Method on Mineralized Products

Three testing groups were included in this section. Ca(NO₃)₂, CaCl₂, and Ca(CH₃COO)₂ were selected as Ca²⁺ sources, and the post-calcium-source method (add Ca²⁺ sources after urea decompose) and pre-calcium-source method (add Ca²⁺ sources before urea decompose) were selected as Ca²⁺ sources addition methods. By means of weighing, multi-parameter analysis, EDS, XRD, and SEM, the production, productivity, and utilization rate of Ca²⁺ source and the substance, phase, morphology, and structure of the mineralized products under different types of Ca²⁺ sources and addition methods were tested in order to determine the most suitable Ca²⁺ source and addition method.

For Group A, 50 mL 1 mol/L urea solution was added to plastic bottles, while for Group B, 50 mL 1 mol/L repair fluid (the mixed solution containing the Ca²⁺ source and urea) was added into plastic bottles. Then, 5 mL OD₆₀₀ = 1.0 *Sporosarcina pasteurii* bacteria solution was added to the plastic bottles for each group. In order to compare the differences between the mineralized products of MICP and chemically synthesized minerals, a third group, Group C, was included. For Group C, 55 mL 1 mol/L mixed solution of CaCl₂ and Na₂CO₃ was added into a plastic bottle. The initial pH values of the three groups were adjusted to 8.0, and the three groups of plastic bottles were placed in a shaking table for 48 h; the temperature was set to 30 °C and the rotating speed was set to 150 r/min. After removal from the shaking table, 1 mol/L Ca²⁺ source solution was immediately added to the plastic bottles belonging to Group A, as shown in Figure 7. The production of mineralized products was measured via the weighing method described above. In addition, the concentration of Ca²⁺ in the mixed solution before and after mineralization was measured using a multi-parameter analyzer, and the samples from each group were dried for further EDS, XRD, and SEM analyses.

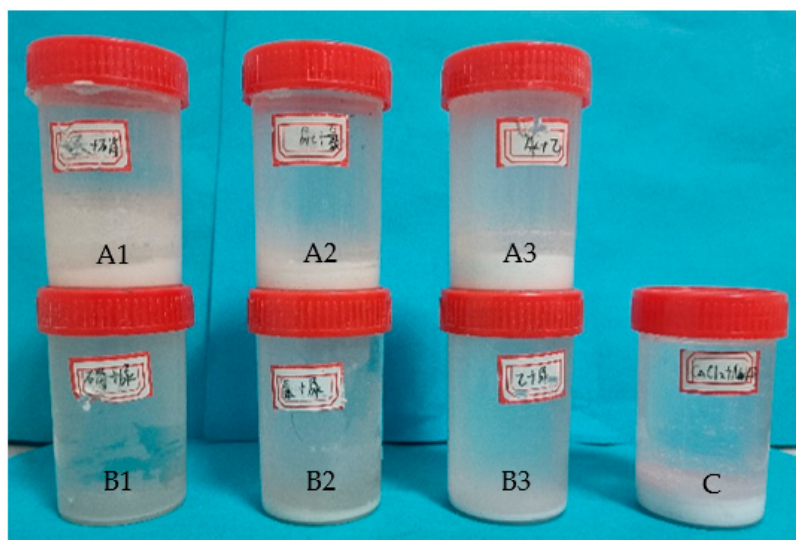


Figure 7. Mineralization with different Ca²⁺ sources and addition methods.

3.2. Results and Discussion

3.2.1. Effect of Ca²⁺ Source and Addition Method on the Characteristics of Mineralized Products and the Mineralization Efficiency

The characteristics, mineral production, mineral productivity, and Ca²⁺ source utilization rate of the mineralized products from each group are shown in Table 3.

Table 3. Sediment properties and mineralization efficiency with different Ca²⁺ sources and addition methods.

Group	Characteristics of Mineralized Products	Mineral Production/g	Mineral Productivity/%	Utilization Rate of Ca ²⁺ Source/%	
A	1. Ca(NO ₃) ₂ , urea, bacteria	Soft, white pastes, white powders after drying	4.658	93.16	93.04
	2. CaCl ₂ , urea, bacteria	Hard, light yellow, bulk, poor integrity	4.754	95.08	94.89
	3. Ca(CH ₃ COO) ₂ , urea, bacteria	Soft, white pastes, white powders after drying	5.005	100.10	98.33
B	1. Ca(NO ₃) ₂ , urea, bacteria	Hard, light yellow, flaky and bulk, good integrity	1.735	34.70	34.46
	2. CaCl ₂ , urea, bacteria	Hard, light yellow, flaky and bulk, good integrity	2.731	54.62	54.35
	3. Ca(CH ₃ COO) ₂ , urea, bacteria	Hard, light yellow flaky and bulk, good integrity	2.210	44.20	42.78
C	CaCl ₂ , Na ₂ CO ₃	Soft, white pastes, white powders after drying	4.680	93.60	93.41

A histogram illustrating the effect of the Ca²⁺ source and addition method on the mineralization efficiency of each group was generated according to the data in Table 3 and is shown in Figure 8.

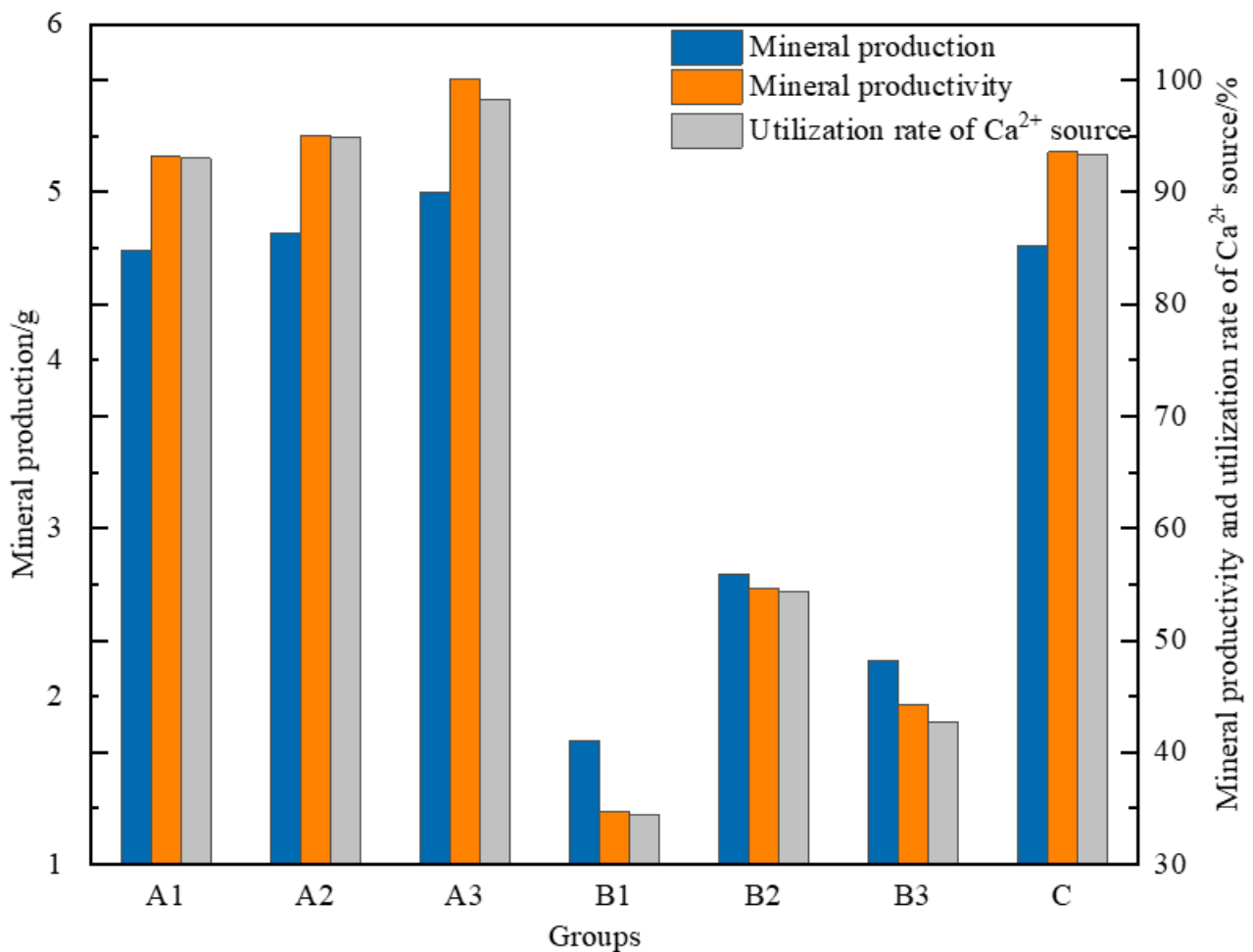


Figure 8. Effect of Ca²⁺ source and addition method on mineralization efficiency.

It can be seen from Table 3 and Figure 8 that the mineralized product characteristics, mineral production, mineral productivity, and Ca^{2+} source utilization rate of Group A and Group C were similar, where both showed higher values than Group B. However, the hardness of the mineralized products was low and their integrity was poor; they appeared as white pastes in solution and white powders after drying.

According to the theory described in Section 2.3, in Group A after 48 h of urea treatment, the urea in the mixed solution was almost completely decomposed and the mixed solution was full of CO_3^{2-} . At this time, the $\alpha_{\text{Ca}^{2+}} \cdot \alpha_{\text{CO}_3^{2-}}$ in the mixed solution instantaneously reached its maximum value with the addition of the Ca^{2+} source, the reaction illustrated in Formula (1) proceeded to the left and the mineral productivity was close to 100%. In Group B, CO_3^{2-} was gradually produced by the decomposition of urea. Although the reaction in Formula (1) proceeded to the left, the $\alpha_{\text{Ca}^{2+}} \cdot \alpha_{\text{CO}_3^{2-}}$ was lower than that in Group A; thus, mineral productivity in Group B was also lower than that in Group A.

Calcite exhibits a trigonal crystal system, where Ca^{2+} ions are located at the top corner and center of each crystal plane and CO_3^{2-} ions are located at the center of each crystal plane and the midpoint of all edges of the crystal cells. Each Ca^{2+} coordinates with six CO_3^{2-} ; that is, the coordination number of Ca^{2+} in calcite is 6. Vaterite exhibits a hexagonal crystal system, where Ca^{2+} and CO_3^{2-} are layered, similar to calcite, but there are two CaCO_3 molecules in each vaterite crystal cell; thus, the coordination number of Ca^{2+} in vaterite is 12 [27,28].

In Group A, the newly added Ca^{2+} combined with CO_3^{2-} in the mixed solution, meeting the coordination number of vaterite; thus, vaterite was generated first. The vaterite crystals were observed to be small, uniform, and powdery. In Group B, while urea was decomposed, the newly produced CO_3^{2-} combined with the existing Ca^{2+} in the mineralizing system, meeting the coordination number of calcite; thus, calcite was generated first. The calcite crystals were observed to be large with certain shapes, and the hardness and integrity were also good.

In the repair of high-temperature concrete damage, the mineralized products should exhibit a certain hardness and integrity. Although the mineral productivity and Ca^{2+} source utilization rate of Group A was much higher than that of Group B, the characteristics of the mineralized products were not suitable; therefore, the optimal method for Ca^{2+} source addition is the post-calcium-source method used in Group B.

Comparing the different types of Ca^{2+} sources in Group B, the mineral productivity and utilization rate were the highest in Group B2; however, the introduction of Cl^- might cause some problems such as steel corrosion, which has adverse effects on steel-reinforced concrete structures. The mineralized products of Group B1 were hard and exhibited good integrity; however, $\text{Ca}(\text{NO}_3)_2$ is flammable and explosive and represents a potential safety hazard in the repair and service processes. Thus, $\text{Ca}(\text{NO}_3)_2$ is not a suitable Ca^{2+} source. In this respect, $\text{Ca}(\text{CH}_3\text{COO})_2$ represented a compromise: the mineral productivity and Ca^{2+} source utilization rate were moderate and the mineralized products were hard and exhibited good integrity. In addition, $\text{Ca}(\text{CH}_3\text{COO})_2$ is safe and environmentally friendly and will not have adverse effects on steel-reinforced concrete. Thus, $\text{Ca}(\text{CH}_3\text{COO})_2$ is an appropriate Ca^{2+} source.

Theoretically, the mineral productivity and utilization rate of the Ca^{2+} source should be equal; that is, the amount of CO_3^{2-} decomposed should be equal to the amount of CO_3^{2-} that combines with Ca^{2+} . However, our results showed that the mineral productivity was slightly higher than the utilization rate of the Ca^{2+} source. This is because CaCO_3 crystals were not the only crystals in the sediments. Due to the different temperatures used during sediment filtration and mineralization, the solubility of different Ca^{2+} sources was also different. There was a small portion of undissolved Ca^{2+} source in the sediments in addition to CaCO_3 crystals. Although the molecular weights of the three types of Ca^{2+} sources used in this experiment were greater than that of CaCO_3 ($\text{Ca}(\text{NO}_3)_2$: 164, CaCl_2 : 111, $\text{Ca}(\text{CH}_3\text{COO})_2$: 158, CaCO_3 : 100), this portion of undissolved Ca^{2+} sources was mistaken

for CaCO₃ with low molecular weight in the process of weighing mineral production; thus, the measured mineral production and the calculated mineral productivity were higher.

3.2.2. EDS Analysis

The energy spectra for each group of samples are shown in Figure 9.

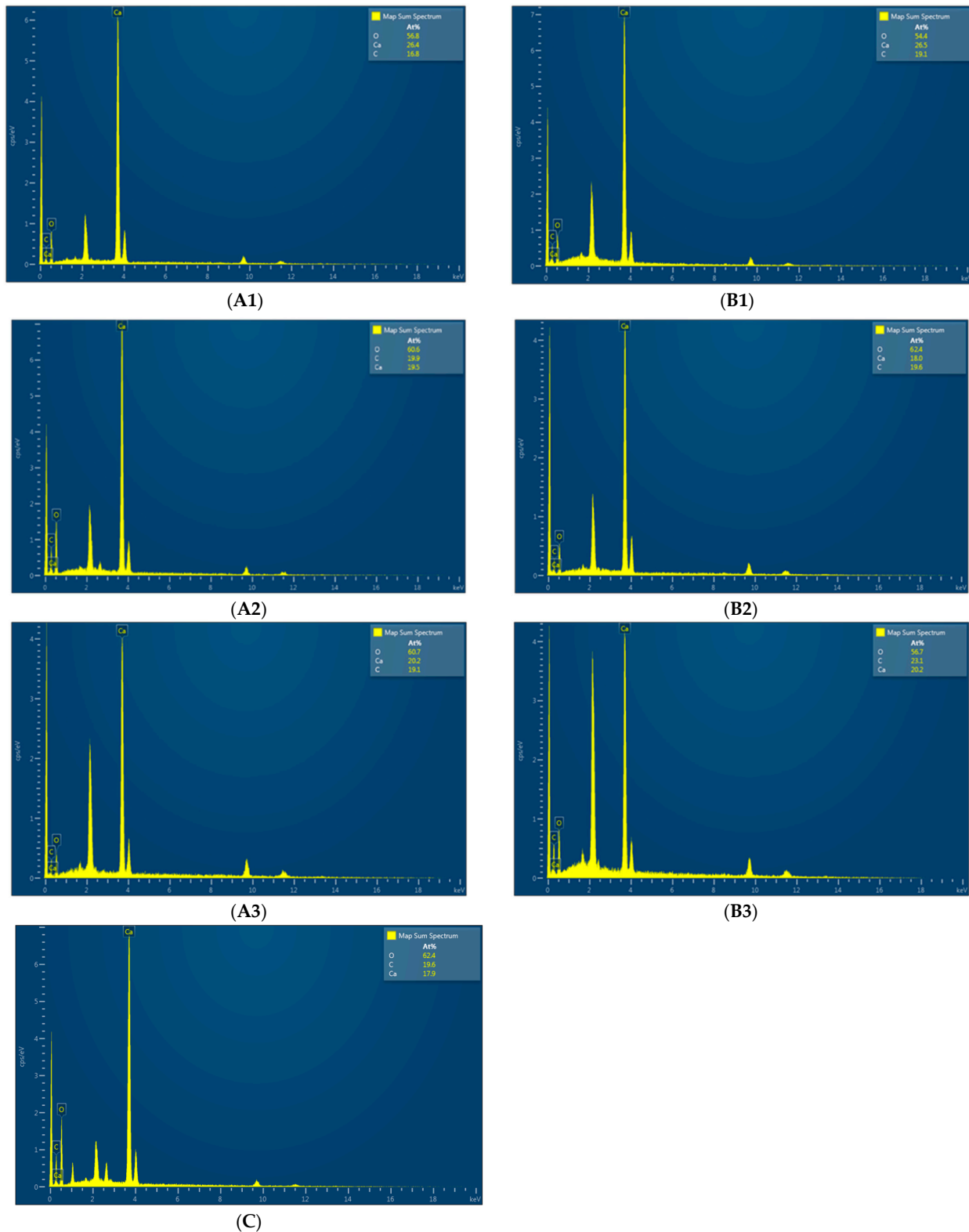


Figure 9. Energy spectra of samples from each group.

The chemical elements and their contents in the samples from each group can be obtained according to Figure 9, as shown in Table 4.

Table 4. Chemical elements and their contents in samples from each group.

Group		Ca	C	O	Total	Ca:C:O Approximate Proportion
A	1	26.4	16.8	56.8	100	1:1:3
	2	19.5	19.9	60.6	100	1:1:3
	3	20.2	19.1	60.7	100	1:1:3
B	1	26.5	19.1	54.4	100	1:1:3
	2	18.0	19.6	62.4	100	1:1:3
	3	20.2	23.1	56.7	100	1:1:3
C		17.9	19.6	62.4	99.9	1:1:3

It can be seen from Figure 9 and Table 4 that the mineralized products of all groups contained Ca, C, and O, and the atomic ratio of the three chemical elements was close to Ca:C:O = 1:1:3; thus, the mineralized products were CaCO₃.

3.2.3. XRD Analysis

The XRD spectrograms of samples from each group are shown in Figure 10.

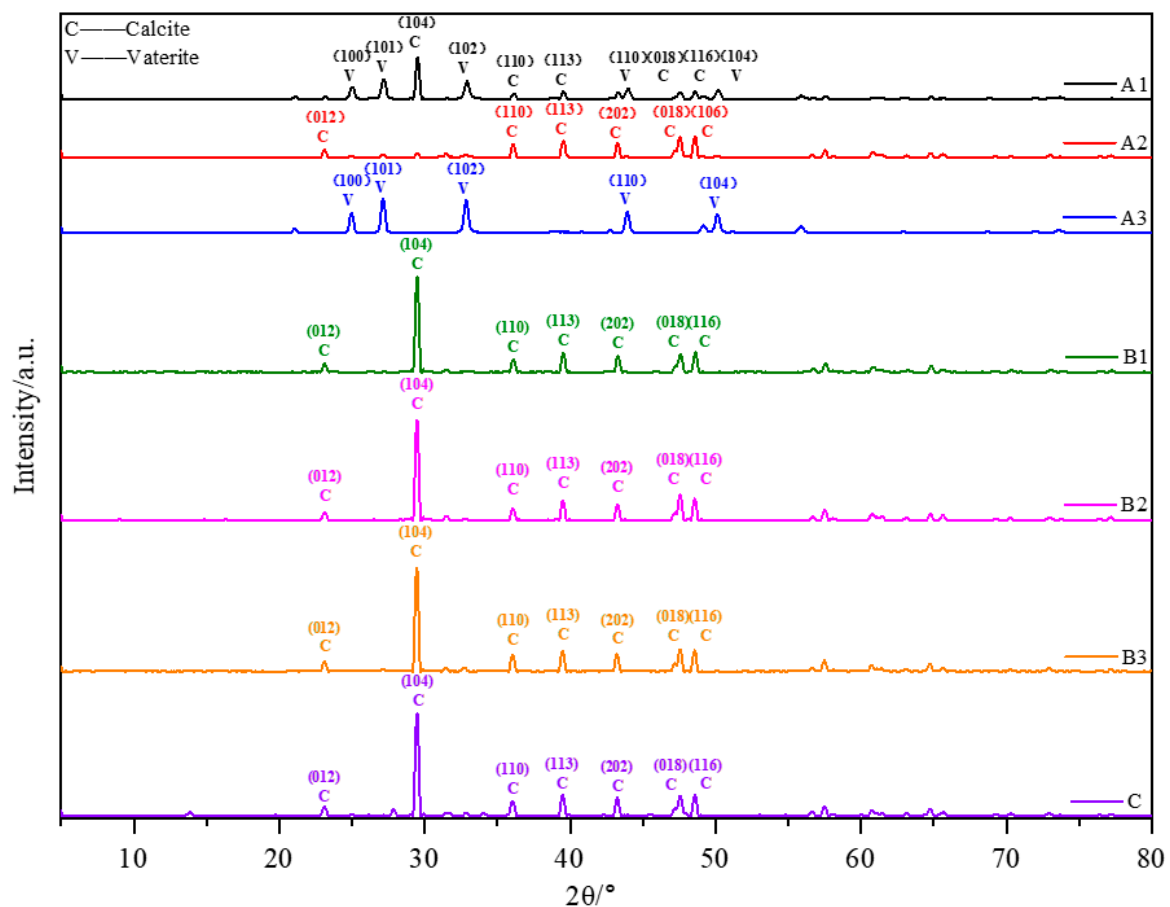


Figure 10. XRD spectrograms of samples from each group.

It can be seen from Figure 10 that the mineralized products of Group B1, B2, B3, and C were all calcite; the mineralized products of Group A1 and A2 were calcite and vaterite; and the products of Group A3 were all vaterite. However, the diffraction peaks of vaterite in Group A2 were not obvious, which was reflected in the output of the JADE 6.5 software.

In Group A1, the mass of calcite accounted for 32.3% of the total mass, while vaterite accounted for 67.7%. In Group A2, the mass of calcite accounted for 52.5% of the total mass, while the mass of vaterite accounted for 47.5%. The mineralized products of the $\text{Ca}(\text{NO}_3)_2$ and CaCl_2 groups were most often calcite, while the mineralized products of the $\text{Ca}(\text{CH}_3\text{COO})_2$ group were unstable, which highlights the differences of Ca^{2+} source addition methods. The mineralized products of the post-calcium-source group were calcite, while the products of the pre-calcium-source group were mostly vaterite.

3.2.4. SEM Observations

The SEM images of samples from each group are shown in Figure 11.

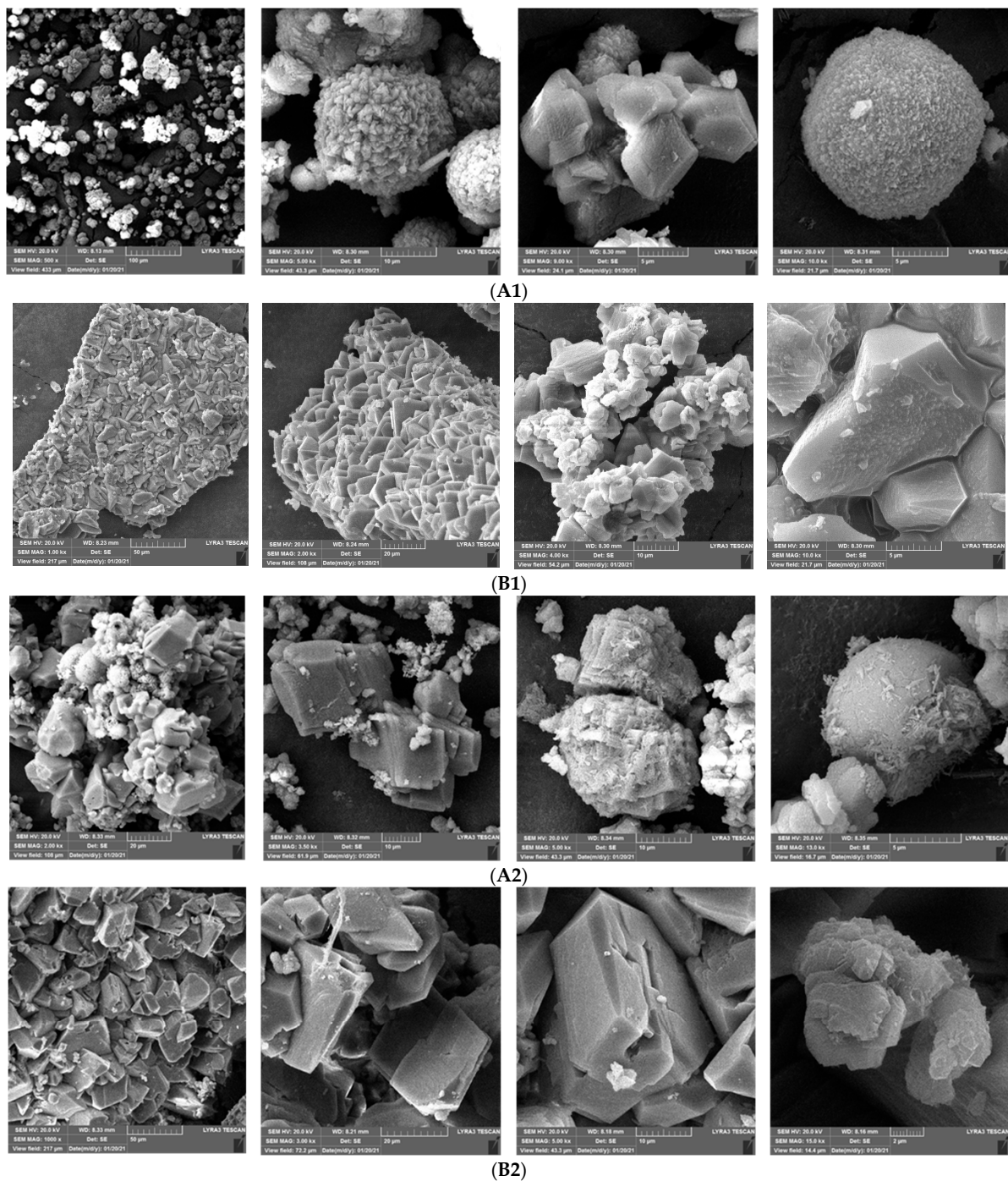


Figure 11. Cont.

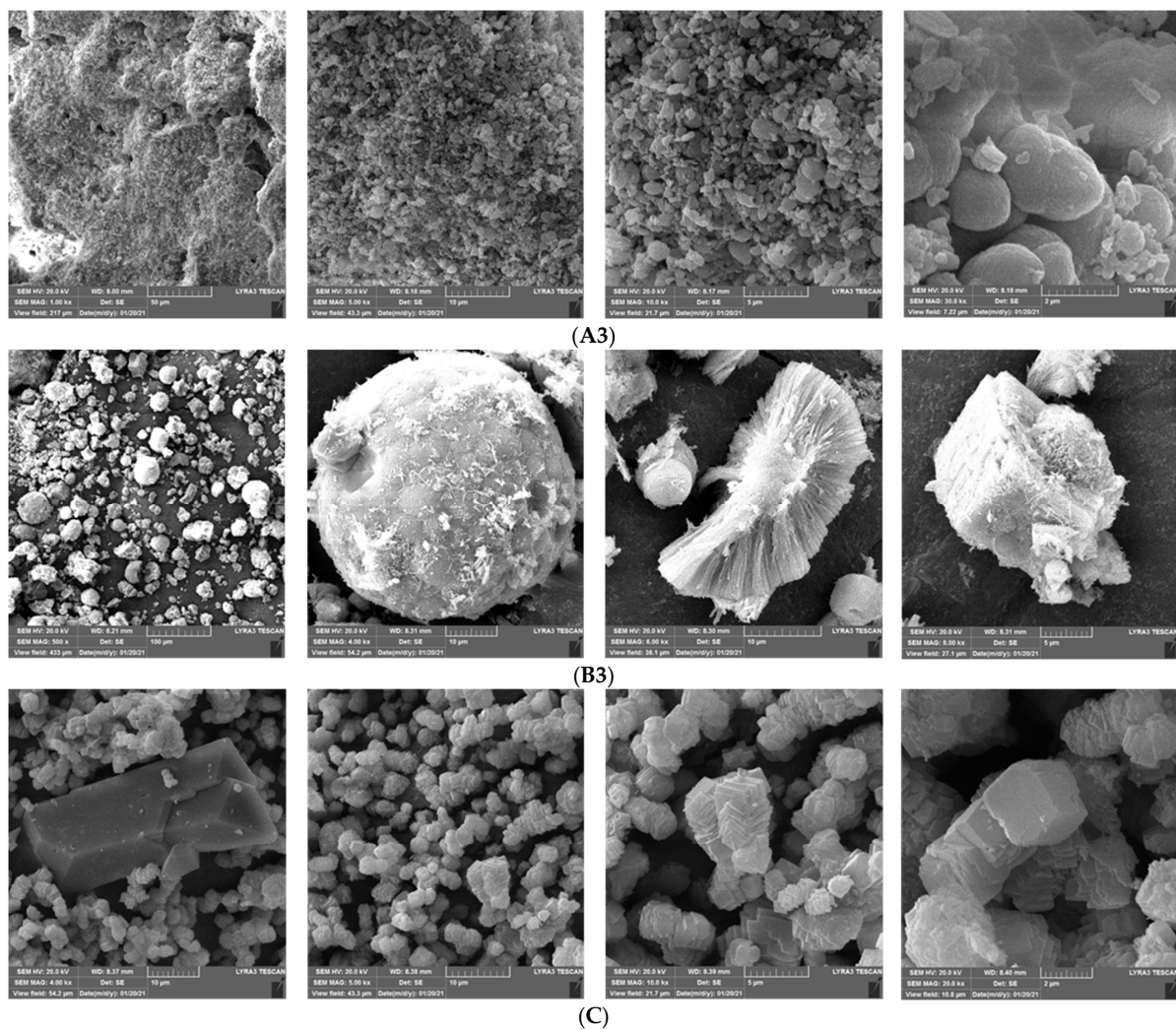


Figure 11. SEM images of samples from each group. (A1) $\text{Ca}(\text{NO}_3)_2$, post-calcium-source method. (B1) $\text{Ca}(\text{NO}_3)_2$, pre-calcium-source method. (A2) CaCl_2 , post-calcium-source method. (B2) CaCl_2 , pre-calcium-source method. (A3) $\text{Ca}(\text{CH}_3\text{COO})_2$, post-calcium-source method. (B3) $\text{Ca}(\text{CH}_3\text{COO})_2$, pre-calcium-source method. (C) $\text{CaCl}_2 + \text{Na}_2\text{CO}_3$.

The morphologies and structures of samples from each group can be observed in Figure 11.

Group A1: Most of the mineralized products were spheres; some were single spheres and some were twin spheres. The size of a single sphere ranged between 5 and 20 μm , while a few large spheres reached 30 μm . The surfaces of the spheres were rough and showed clusters of triangular ‘scales’, indicating that these spheres were formed by the growth of these triangular crystals from the center to the surface. In addition, there were a few hexahedral crystals with a size of 5 μm .

Group B1: Most of the mineralized products were triangular flat plates with sizes ranging from 5 to 20 μm . The surfaces of most of the triangular crystals were smooth, although there were irregular crystals attached to some of the triangular crystals. In addition, there were some irregular flat plates between 15 and 20 μm , slightly larger than the triangular flat plates, with irregularly shaped crystals attached to their surface. When the magnification was increased, it was observed that the triangular flat plates were not actually flat plates but rather blocks.

Group A2: The mineralized products mainly took on three shapes: sphere, hexahedron, and irregular. The spheres were 5~20 μm , exhibiting rough surfaces with irregular crystals attached. The hexahedrons were 10~20 μm with smooth surfaces; some also had irregular

crystals attached. The irregular crystals exhibited different shapes and sizes ranging from 1 to 10 μm ; some of them were floccule, while others were ‘cotton’ shaped.

Group B2: The mineralized products were mostly polyhedral crystals between 20 and 40 μm with smooth surfaces. In addition, there were some individual tetrapyramidal crystals with sizes of 10~25 μm ; the surfaces of these crystals were also smooth.

Group A3: The mineralized products were mostly spheres with sizes of 0.5~2.5 μm . The surface of these crystals was smooth, where some were twin spheres and others formed spherical aggregates.

Group B3: The mineralized products were mostly single spheres with a size of 2~40 μm and rough surfaces, and irregular crystals were also attached to some spheres. A broken sphere was also observed, from which spherical crystals were formed via radiative growth from the center to the surface. In addition, we also observed a hexahedron surrounded by a sphere of 10 μm with a rough surface and irregular crystals attached.

Group C: The mineralized products were mostly square flaky aggregates with a size of 2~3 μm and a smooth surface. In addition, there were a few 2 μm cubes and 25 μm pyramids.

According to the conclusions from Sections 2.2 and 3.2.3, the mineralized products in Group B1, B2, B3, and C were all calcite; the mineralized products in Group A1 and A2 were calcite and vaterite; and the mineralized products in Group A3 were all vaterite. The calcite exhibited different morphologies, including triangle, polyhedron, sphere, square flaky aggregates, and pyramids, while the vaterite crystals were mostly spherical aggregates.

In conclusion, $\text{Ca}(\text{CH}_3\text{COO})_2$ was found to be an optimal Ca^{2+} source while the pre-calcium-source method was determined as the most appropriate addition method.

4. Verification of Repair Effect

4.1. Preparation and Treatment of Specimen

4.1.1. Materials

The raw materials in this section include urea analytical reagent (Fuchen Chemical Reagent Co., Ltd., Tianjin, China), calcium acetate analytical reagent (Fuchen Chemical Reagent Co., Ltd., Tianjin, China), P.O 42.5 ordinary portland cement (Shuangliang Concrete Co., Ltd., Taiyuan, China), 5~26.5 mm continuously and well-graded crushed stone (Huiyong Sand and Stone Co., Ltd., Taiyuan, China), II area medium sand with fineness modulus of 2.86 (Huiyong Sand and Stone Co., Ltd., Taiyuan, China), and polycarboxylate superplasticizer (China West Construction Group Co., Ltd., Urumqi, China) with a water-reducing rate 20%.

C50 concrete is often used in buildings and structures, and it was also used in this study. The mix proportion of C50 concrete is shown in Table 5, the performance of cement is shown in Table 6, the performance of gravel is shown in Table 7, the performance of sand is shown in Table 8, and the performance of superplasticizer is shown in Table 9.

Table 5. Mix proportion of C50 concrete.

Cement/(kg/m ³)	Water/(kg/m ³)	Aggregate/(kg/m ³)	Sand/(kg/m ³)	Superplasticizer/(kg/m ³)	w/b	Slumps/mm
430	165	1130	720	1.15	0.38	152

Note: The mix proportion of C50 concrete is designed according to JGJ55-2011 [29].

Table 6. Performance of cement.

Test Items	Specific Surface Area/(m ² /kg)	Loss on Ignition/%	Stability	Setting Time/min		Compressive Strength/MPa		Flexural Strength/MPa	
				Initial Setting	Final Setting	3 Days	28 Days	3 Days	28 Days
Technical standard	≥ 300	≤ 5.0	boiling process qualified	≥ 45	≤ 600	≥ 17.0	≥ 42.5	≥ 3.5	≥ 6.5
Result	366	3.9		70	470	25.5	48.5	5.4	7.6

Note: The cement used in this study follows GB 175-2007 [30].

Table 7. Performance of gravel.

Test Items	Apparent Density/(kg/m ³)	Bulk Density/(kg/m ³)	Voidage/%	Mud Content/%	Clay Content/%	Needle or Plate Content/%	Crushing Value/%
Technical standard	≥2600	-	≤45.0	≤1.0	≤0.5	≤15	≤10
Result	2680	1760	34.60	0.68	0.10	7	9

Note: The gravel used in this study follows JGJ 52-2006 [31].

Table 8. Performance of sand.

Test Items	Apparent Density/(kg/m ³)	Bulk Density/(kg/m ³)	Methylene Blue	Powder Content/%	Voidage/%	Mass Loss/%	Fineness Modulus
Technical standard	≥2500	≥1400	<1.4	≤10.0	≤44.0	≤8	2.3~3.0
Result	2750	1673	1.2	7.61	38.44	6.00	2.86

Note: The gravel used in this study follows JGJ 52-2006 [31].

Table 9. Performance of superplasticizer.

Test Items	Water Reducing Rate/%	Density/(g/mL)	Solid Content/%	Fluidity of Cement Grout/mm	pH	Chloride Content/%	Alkali Content/%
Technical standard	≥25	1.09 ± 0.02	22 ± 2	≥250 (w/b = 0.29)	6~8	≤0.02	≤0.2
Result	20	1.1	21	265	8	0.01	0.09

Note: The superplasticizer used in this study follows JGJ 56-84 [32].

4.1.2. Preparation and Cure of Specimens

40 mm cube specimens were cast and cured in accordance with GB/T 50081-2019 [33] and GB/T 50082-2009 [34]. The concrete specimens were cast by a UJZ-15 concrete mixer (HangJianHuaYe S&T Development Co., Ltd., Beijing, China), and the rotational speed was 45 r/min. The mixer was made wet by cement mortar with the same w/b ratio first, gravel and sand were added into the mixer and mixed evenly, cement went next, and the mixtures were continued mixed for two minutes. Then the mixed solution of water and superplasticizer was poured into the mixer, another two minutes were needed. At last, the mixtures were poured out, and the slump was measured. Afterward, the mixtures were loaded into molds, placed on a shaking table for vibration, and then placed in an environment with a temperature of 20 ± 5 °C. After 24 h, the formed specimens were de-molded and put in saturated Ca(OH)₂ solution with a temperature of 20 ± 2 °C for curing. The specimens were taken out for testing after 28 days.

4.1.3. High-Temperature Treatment

The concrete specimens were divided into five groups: ambient temperature, 300 °C, 400 °C, 500 °C, and 600 °C, respectively. A thermocouple was embedded in the center of one specimen in each group. A muffle furnace was used to heat the specimens. The temperature increasing rate was set as 10 °C/min. The temperature in the center of the specimens could be obtained by a temperature inspection instrument outside the muffle furnace. When the temperature shown on the temperature inspection instrument reached 300 °C, 400 °C, 500 °C, and 600 °C, respectively, the center of the specimens reached the corresponding temperature, the temperature was maintained for 30 min, then the muffle furnace was turned off, the furnace door was opened for natural cooling, as shown in Figure 12.

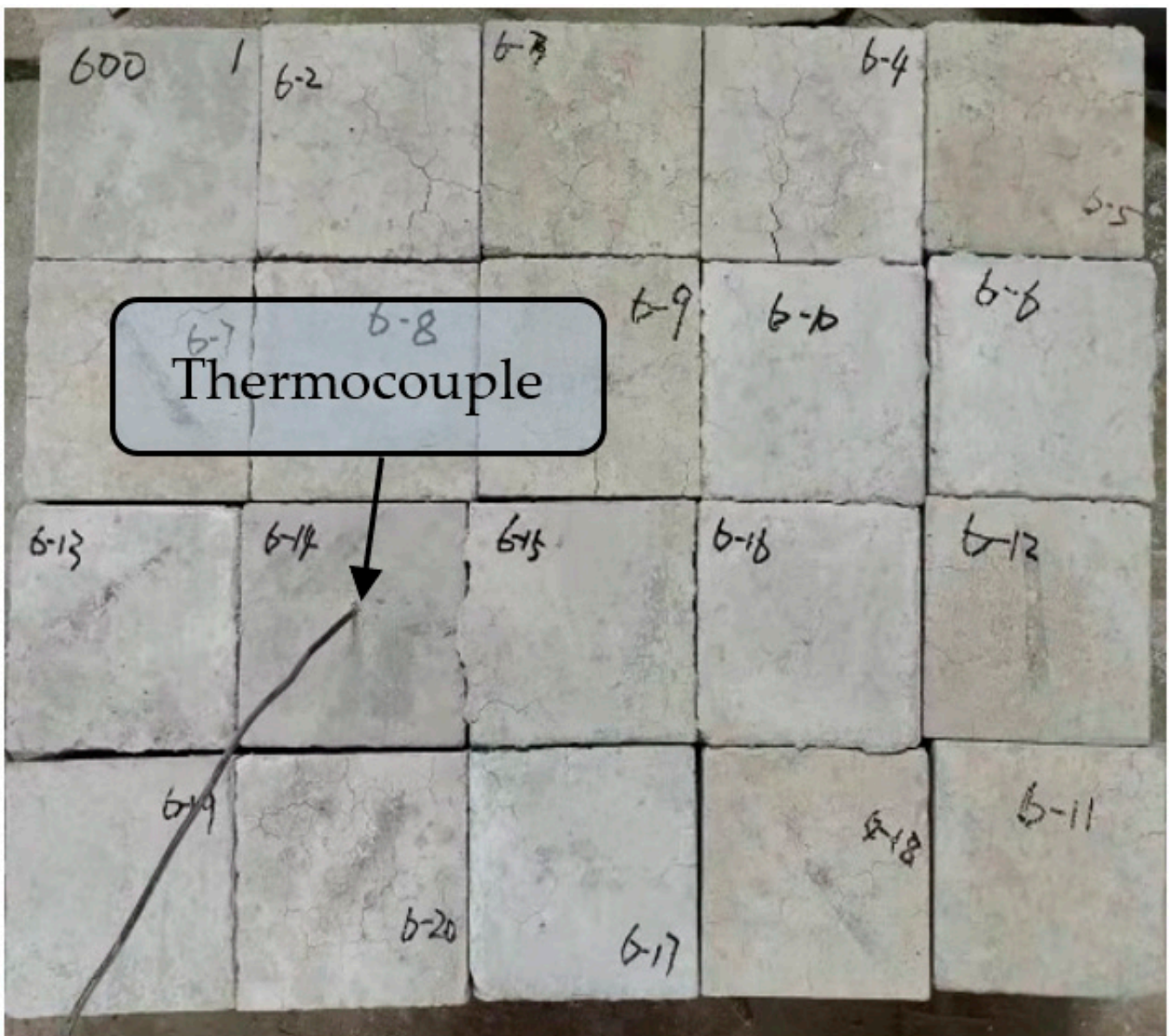


Figure 12. High-temperature treatment of concrete specimens.

4.2. Repair Method

The MICP technology was then adopted to repair high-temperature concrete damage. For this, 40 mm cube specimens were taken as repair objects; *Sporosarcina pasteurii* were taken as the repair tool; urea and $\text{Ca}(\text{CH}_3\text{COO})_2$ were mixed as repair fluid with a concentration of 1 mol/L, the Ca^{2+} source addition method was selected according to previous experiments; and the immersion repair method was used, as shown in Figure 13. The repair effect was evaluated through compressive strength and water absorption.

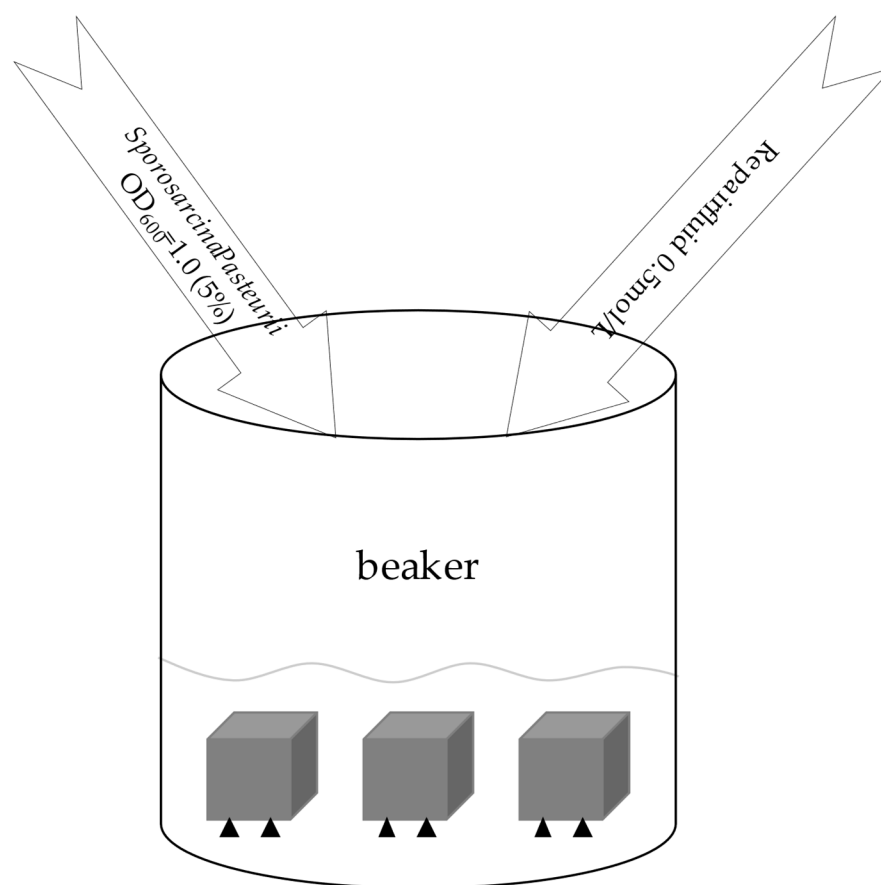


Figure 13. Process of immersion method. Note: The water-based repair fluid may cause rehydration in damaged concrete, but it was not considered in this study.

4.3. Compressive Strength

The compressive strengths of the specimens before and after repair were tested by a YAW-300C compression testing machine (Liling Testing Machine Co., Ltd., Jinan, China) in accordance with GB/T 50081-2019 [33], three specimens in each group, the loading rate was set as 0.5 MPa/s, the results are shown in Table 10.

Table 10. Compressive strength of concrete specimens under different conditions.

Damage Temperature/°C	Undamaged/MPa	Damaged/MPa	Repaired/MPa
300	67.15	56.74	56.87
400	67.15	51.93	53.33
500	67.15	44.17	51.31
600	67.15	16.04	48.55

It can be seen from Table 10 that at 300, 400, 500, and 600 °C, the compressive strength of the repaired specimens increased by 0.23%, 2.7%, 16.16%, and 202.68% compared with the damaged specimens and reached 84.69%, 79.42%, 76.41% and 72.3% of that of the undamaged specimens, respectively. When the damage temperature was low, the compressive strength of the repaired specimens was not significantly improved. On the other hand, when the damage temperature was high, the compressive strength of the repaired specimens showed significant improvement.

4.4. Water Absorption

The water absorption of the concrete specimens before and after repair was tested in accordance with GB/T 11969-2020 [35], the process for the water absorption test is shown in Figure 14, and the results are shown in Table 11.

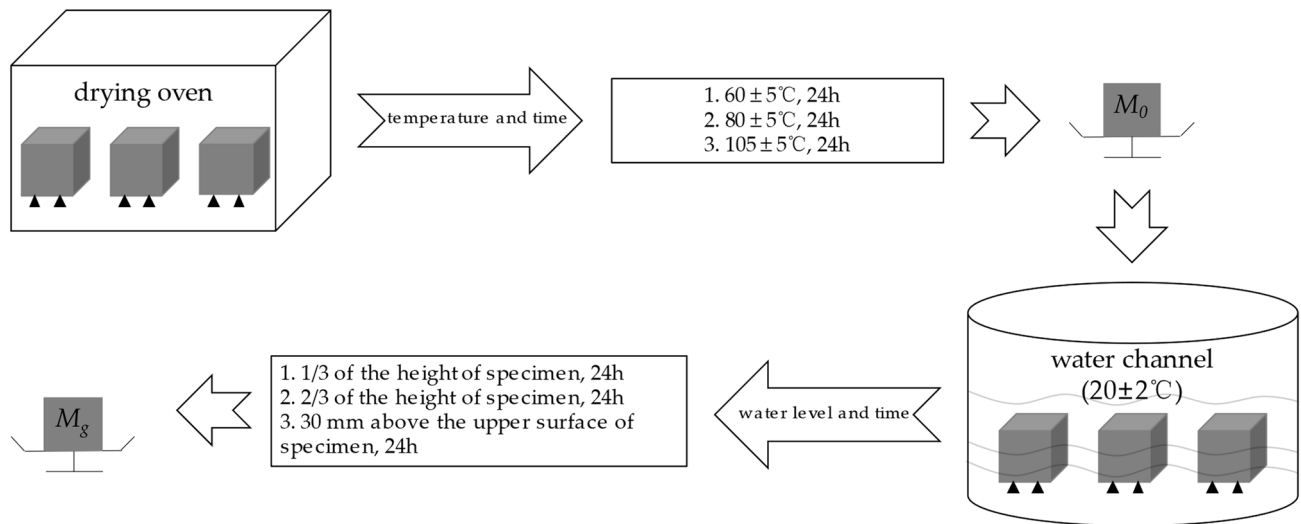


Figure 14. Process of water absorption test.

Table 11. Water absorption of concrete specimens under different conditions.

Damage Temperature/°C	Undamaged/%	Damaged/%	Repaired/%
300	3.81	4.87	3.77
400	3.81	5.09	3.87
500	3.81	5.6	3.98
600	3.81	6.44	4.23

It can be seen from Table 11 that at 300, 400, 500, and 600 °C, the water absorption of the repaired specimens was 22.59%, 23.97%, 28.93%, and 34.32% lower than that of the damaged specimens, and 1.05%, 1.57%, 4.46% and 11.02% higher than that of the undamaged specimens, respectively. Under high temperatures, both the surface and interior of the specimens were seriously damaged, which was more conducive to the mineralizing system entering the specimens through the surface defects and flowing into the interior through the penetrating cracks.

In conclusion, the compressive strength showed a certain degree of recovery, while the water absorption exhibited a certain degree of reduction at each damage temperature. Overall, the higher the damage temperature, the more obvious the repair effect.

5. Conclusions and Prospect

This study extended the MICP technique to the field of high-temperature concrete damage repair, and filled the research gaps of the influences of calcium source types and calcium source addition methods on mineralization products in MICP. In this work, the influences of calcium source types and calcium source addition methods on the mineralization products were studied, and the regulatory mechanism of calcium source types and calcium source addition methods on the mineralization products was revealed. The appropriate calcium source and calcium source addition method were determined, and the repair effect of MICP on high-temperature concrete damage was verified. Based on the results achieved during this study, the following conclusions are drawn:

- (1) The mineralized products of *Sporosarcina pasteurii* were white suspended pastes in solution and white powders after drying. Our analysis showed that the products were

- CaCO₃, containing mixed crystals of vaterite and calcite, most of which were spheres and some of which were irregular shapes.
- (2) With all kinds of Ca²⁺ sources and all addition methods, the mineralized products were CaCO₃. The mineralized products of the Ca(NO₃)₂ and CaCl₂ groups were more inclined to form calcite, while the mineralized products of the Ca(CH₃COO)₂ group were unstable. This also depended on the method used to add the Ca²⁺ source. The mineralized products of the post-calcium-source group were calcite, while those of the pre-calcium-source group were more inclined to form vaterite. The calcite morphologies were different, while the vaterite crystals were mostly spherical aggregates. Overall, Ca(CH₃COO)₂ was the most suitable Ca²⁺ source, while the pre-calcium-source addition method provided the most optimal results.
 - (3) At each damage temperature, the compressive strength showed a certain degree of recovery, while the water absorption exhibited a certain degree of reduction, indicating that MICP resulted in an improvement in the mechanical properties and durability of the damaged concrete. The higher the damage temperature, the more obvious the repair effect.

This study has guiding significance for the application of MICP in repairing high-temperature concrete damage. However, the actual application effect requires further examination. Firstly, mineralization conditions. Except for the types of calcium source and the calcium source addition methods, temperature, pH value, bacterial solution concentration, and repair fluid concentration also affect the mineralization process; however, the influences of mineralization conditions on mineralization products have not been studied in this work. Secondly, the repair method. The immersion repair method in this study can be used in the laboratory, but it is difficult to apply in practical engineering. For concrete structural components in practical engineering, our idea is to fix molds outside the components, and fill the gaps between the molds and the components with repair fluid, the repair fluid was pressed into the concrete cracks as much as possible by air pressure externally, or using an external vacuum pump to vacuum the gaps between the molds and the components before the repair fluid was inhaled. However, these are only possible ideas at present, the repair effect of these methods needs to be examined in further studies in practical engineering. Thirdly, rehydration of water. The water-based repair fluid in Figure 13 may cause rehydration in damaged concrete, also recovering the mechanical properties and durability of damaged concrete. However, it was not considered in this study. This is the limitation of our study, the rehydration of cementitious matrix should be taken into consideration in further studies. Finally, repair effect at a lower temperature. The repair effect below 500 °C was not so obvious. It needs further study to improve the repair effect when the temperature is not so high. If these issues have been addressed, MICP will have a broad prospect in more fields in the near future.

Author Contributions: Writing—original draft: H.W.; Writing—review and editing: H.W. and Y.F.; Data curation: H.W. and X.W.; Methodology: H.D. and R.L.; Formal analysis: X.W.; Investigation: Y.F. and X.W.; Conceptualization: H.W. and X.W.; Resources: R.L.; Supervision: Y.F.; Project administration: H.D. All authors have read and agreed to the published version of the manuscript.

Funding: This research was funded by the Key Research and Development (R&D) Projects of Shanxi Province, China (No. 201903D321113).

Institutional Review Board Statement: Not applicable.

Informed Consent Statement: Not applicable.

Data Availability Statement: The data presented in this study are available from the corresponding author.

Acknowledgments: The authors sincerely thank Xiaowei Yang for his contributions to the data processing of this research.

Conflicts of Interest: The authors declare no conflict of interest.

References

1. Wu, B.; Yuan, J.; Wang, G. Experimental Research on The Mechanical Properties of HSC after High Temperature. *China Civ. Eng. J.* **2000**, *33*, 8–12, 34. [[CrossRef](#)]
2. Gao, R.; Xu, Q.; Li, X.; Wang, Q.; Yu, L. Experimental Research on Resistance of Concrete to Chloride Penetration after High Temperature. *J. Build. Mater.* **2014**, *17*, 690–694. [[CrossRef](#)]
3. Du, H.; Fan, Y. Meso-Structure Damage of C60 High Performance Concrete at High Temperature Based on X-CT. *J. Build. Mater.* **2020**, *23*, 210–215. [[CrossRef](#)]
4. Rabehi, B.; Ghernouti, Y.; Li, A.; Boumchedda, K. Comparative behavior under compression of concrete columns repaired by fiber reinforced polymer (FRP) jacketing and ultra high-performance fiber reinforced concrete (UHPFRC). *J. Adhes. Sci. Technol.* **2014**, *28*, 2327–2346. [[CrossRef](#)]
5. Chen, X.; Zhang, Y.; Li, S.; Geng, Y.; Hou, D. Influence of a New Type of Graphene Oxide/Silane Composite Emulsion on the Permeability Resistance of Damaged Concrete. *Coatings* **2021**, *11*, 208. [[CrossRef](#)]
6. Du, H. *New Methods for Fire Damage Detection and Evaluation of Reinforced Concrete Structures*, 1st ed.; Chemical Industry Press: Beijing, China, 2018.
7. Chen, W. Multi-Scale Study on Defects of High Strength and High Performance Concrete at High Temperature. Master's Thesis, Taiyuan University of Technology, Taiyuan, China, 2018.
8. Wang, R. Study on Biomineralization Process of Calcium Carbonate Mediated by Microbe and Its Application in Restoration of Cement-Based Materials Defects. Ph.D. Thesis, Southeast University, Nanjing, China, 2009.
9. Duan, J.; Fang, H.; Lin, J.; Chen, J.; Wei, S.; Ye, Z. Nutrient Removal from Swine Wastewater by Struvite Precipitation with Ammonia Adsorption on Zeolite. *Environ. Sci. Technol.* **2011**, *34*, 181–184. [[CrossRef](#)]
10. Kong, J.; Chen, P.; Huang, S.; Li, Q.; Xu, H. Experimental Investigation on Solidifying The Desert Aeolian Sand Undercombined Action of MICP and Vegetation. *J. Zhejiang Sci. Tech. Univ.* **2019**, *41*, 688–696. [[CrossRef](#)]
11. Li, C.; Tian, L.; Dong, C.; Zhang, Y.; Wang, Y. Experimental Study of Zinc-Lead Composite Contaminated Soil Solidified/Stabilized by MICP Technology Combined with Porous Silicon Adsorption Materials. *Rock Soil Mech.* **2022**, *43*, 307–316. [[CrossRef](#)]
12. Zhu, W. Fundamental Studies of Calcium Carbonate Mineralization Induced by Microbiologically in Stone Materials Surface Protection. Master's Thesis, Southwest University of Science and Technology, Mianyang, China, 2011.
13. Wang, J.; Soens, H.; Verstraete, W.; De Belie, N. Self-healing concrete by use of microencapsulated bacterial spores. *Cem. Concr. Res.* **2013**, *56*, 139–152. [[CrossRef](#)]
14. Ortega-Villamagua, E.; Gudiño-Gomezjurado, M.; Palma-Cando, A. Microbiologically Induced Carbonate Precipitation in the Restoration and Conservation of Cultural Heritage Materials. *Molecules* **2020**, *25*, 5499. [[CrossRef](#)]
15. Zhang, Y. Research on Sand Cementation and Concrete Cracks Repairment by Microbially Induced Carbonate Precipitation Technology. Master's Thesis, Tsinghua University, Beijing, China, 2014.
16. Fan, Y. Study on Mechanism and Multi-Scale Performance of Biomineralization for Repairing Fire Damage of Concrete. Ph.D. Thesis, Taiyuan University of Technology, Taiyuan, China, 2022.
17. Whiffin, V.S. Microbial CaCO₃ Precipitation for the Production of Biocement. Ph.D. Thesis, Murdoch University, Perth, Australia, 2004.
18. Green, D.C.; Shida, Y.; Honma, N.; Holden, M.A.; Kim, Y.-Y.; Kulak, A.N.; Ogasawara, W.; Meldrum, F.C. Skin-Deep Surface Patterning of Calcite. *Chem. Mater.* **2019**, *31*, 8725–8733. [[CrossRef](#)]
19. Jones, B. Review of aragonite and calcite crystal morphogenesis in thermal spring systems. *Sediment. Geol.* **2017**, *354*, 9–23. [[CrossRef](#)]
20. Nehrke, G.; Van Cappellen, P. Framboidal vaterite aggregates and their transformation into calcite: A morphological study. *J. Cryst. Growth* **2006**, *287*, 528–530. [[CrossRef](#)]
21. Ahmed, J.; Menaka; Ganguli, A.K. Controlled growth of nanocrystalline rods, hexagonal plates and spherical particles of the vaterite form of calcium carbonate. *Crystengcomm* **2009**, *11*, 927–932. [[CrossRef](#)]
22. Brečević, L.; Nielsen, A.E. Solubility of amorphous calcium carbonate. *J. Cryst. Growth* **1989**, *98*, 504–510. [[CrossRef](#)]
23. Kralj, D.; Brečević, L.; Nielsen, A.E. Vaterite growth and dissolution in aqueous solution I. Kinetics of crystal growth. *J. Cryst. Growth* **1990**, *104*, 793–800. [[CrossRef](#)]
24. Wang, H.; Wu, X.; Qiu, X.; Liu, D. Microbially Induced Carbonate Precipitation: A Review. *Microbiol. China* **2013**, *40*, 180–189. [[CrossRef](#)]
25. Rhee, S.-H.; Lee, J.D.; Tanaka, J. Nucleation of Hydroxyapatite Crystal through Chemical Interaction with Collagen. *J. Am. Ceram. Soc.* **2004**, *83*, 2890–2892. [[CrossRef](#)]
26. Zhang, X.; Yu, P.; Luo, Y. Study on Kinetics of Formation of CaCO₃ Crystal by Solution Conductivity Measurement. *Chin. J. Appl. Chem.* **2004**, *21*, 187–191. [[CrossRef](#)]
27. Wang, J.; Zhang, Q.; Qiu, Y.; Li, L.; Ye, J.; Cui, W. The First Principles of The Crystal Structure and Active Sites of Calcite. *Chin. J. Eng.* **2017**, *39*, 487–493. [[CrossRef](#)]
28. Jiang, J.; Wu, Y.; Yao, Y.; Gao, S.; Zhang, C.; Shen, T.; Liu, J. Progress in Tuning of Metastable Vaterite Calcium Carbonate. *J. Inorg. Mater.* **2017**, *32*, 681–690. [[CrossRef](#)]
29. *JGJ 55-2011*; Specification for Mix Proportion Design of Ordinary Concrete. China Architecture & Building Press: Beijing, China, 2011.

30. *GB175-2007*; Common Portland Cement. Standards Press of China: Beijing, China, 2007.
31. *JGJ 52-2006*; Standard for Technical Requirements and Test Method of Sand and Crushed Stone (or Gravel). China Architecture & Building Press: Beijing, China, 2006.
32. *JGJ 56-84*; Water Reducing Admixture Used for Concrete-Quality Requirements and Testing Methods. China Architecture & Building Press: Beijing, China, 1984.
33. *GB/T 50081-2019*; Standard for Test Methods of Concrete Physical and Mechanical Properties. China Architecture & Building Press: Beijing, China, 2019.
34. *GB/T 50082-2009*; Standard for Test Methods of Long-Term Performance and Durability of Ordinary Concrete. China Architecture & Building Press: Beijing, China, 2009.
35. *GB/T 11969-2020*; Test Methods of Autoclaved Aerated Concrete. Standards Press of China: Beijing, China, 2020.

Disclaimer/Publisher's Note: The statements, opinions and data contained in all publications are solely those of the individual author(s) and contributor(s) and not of MDPI and/or the editor(s). MDPI and/or the editor(s) disclaim responsibility for any injury to people or property resulting from any ideas, methods, instructions or products referred to in the content.